High-precision X-ray polarimeter based on channel-cut crystals

Shang-Yu Si[1,2,3] Zhong-Liang Li[1,2,3*] Wen-Hong Jia[1,2,3*] Lian Xue[3] Hong-Xin Luo[1,2,3]

Jian-Cai Xu[4] Bai-Fei Shen[2,4] Lin-Gang Zhang[2,4] Liang-Liang Ji[2,4]

Yu-Xin Leng[2,4*] Ren-Zhong Tai[1,2,3*]

[1]Shanghai Institute of Applied Physics, Chinese Academy of Sciences, Shanghai 201800, China

[2]University of Chinese Academy of Sciences, Beijing 100049, China

[3]Shanghai Synchrotron Radiation Facility, Shanghai Advanced Research Institute, Chinese Academy of Sciences, Shanghai 201204, China

[4]Shanghai Institute of Optics and Fine Mechanics, Chinese Academy of Sciences, Shanghai 201800, China

Abstract: We report on using synthetic silicon for a high-precision X-ray polarimeter comprising a polarizer and an analyzer, each based on a monolithic channel-cut crystal used at multiple Brewster reflections with a Bragg angle very close to 45°. Experiments were performed at the BL09B bending magnet beamline of the Shanghai Synchrotron Radiation Facility using a Si(800) crystal at an X-ray energy of 12.914 keV. A polarization purity of 8.4×10^{-9} was measured. This result is encouraging, as the measured polarization purity is the best-reported value for the bending magnet source. Notably, this is the firstly systematic study on the hard X-ray polarimeter in China, which is crucial for exploring new physics, such as verifying vacuum birefringence.

Keywords: X-ray polarimeter, Vacuum birefringence, Synchrotron radiation, Channel-cut crystal

1 Introduction

Polarization is a fundamental characteristic of electromagnetic waves. The discovery of X-ray polarization by Barkla in 1904 [1] was decisive in its identification as electromagnetic waves, and polarized X-rays have enabled many applications. Today, high-precision polarization modulation and measurement of X-rays are significant techniques in synchrotron radiation (SR) applications, particularly for resonant/non-resonant X-ray scattering [2-5] and nuclear resonant X-ray scattering experiments [6,

7], as they can provide deep insights into the structure of materials via X-ray dichroism [8, 9], as well as detect novel physics phenomena such as vacuum birefringence [10-13], which was initially predicted in the early days of quantum electrodynamics (QED) [14]. The key to the above experiments was obtaining X-rays with ultrahigh polarization purity, defined as the ratio of the polarized components parallel and normal to the diffraction plane integrated over a certain angular and energy range [15].

Realizing the first X-ray diffraction experiments based on crystals [16] and developing the diffraction theory [17] laid the foundation for effectively modulating the polarization of X-rays. In 1961, Cole et al. utilized the Borrmann effect in perfect crystals to obtain linearly polarized X-rays and created the first crystal polarimeter [18]. Nonetheless, the polarization purity based on the Borrmann effect is limited to the 1% level because of the problems of modulation efficiency and absorption [19]. Consequently, there has been a dearth of systematic studies on X-ray polarization over the past 30 years. Since the 1990s, high-precision X-ray polarimeters [20-24] based on the Bragg diffractions of perfect crystals have made tremendous strides, benefiting from advancements in SR sources and crystal processing technology. In 1990, an extinction ratio of 10^6 was achieved near the cobalt K-edge using a white SR beam from a bending magnet (BM) source [20]. In 1997, a polarization purity of 4×10^{-8} at 14.4 keV was achieved using an asymmetrically cut Si(840) crystal [21]. In 2011, B. Marx et al. employed four reflections of a channel-cut crystal with a Bragg angle fairly close to 45° to reach a polarization purity of 9×10^{-9} at 12.914 keV and 1.5×10^{-9} at 6.457 keV [22], and two years later, this result was elevated to an order of 10^{-10} [23]. Currently, the best polarization purity of X-rays could approach 8×10^{-11} attained at an X-ray free-electron laser (XFEL) [24], which has met the demands to explore new physics, such as the experimental verification of vacuum birefringence [13].

With the progress of accelerator [25-28] and laser technology in recent years [29-31], new-generation accelerator light sources with ultrahigh brightness, and ultra-intense lasers with ultrashort pulses are already being made, which will establish a solid foundation for exploring new physics in the future. However, related research on X-ray polarimeters, one of the key technologies in pump-probe experiments, is almost absent

in China. Therefore, developing a high-precision X-ray polarimeter that can be used in related experiments is highly desirable. A high-quality accelerator light source is required to develop high-precision X-ray polarimeters. The Shanghai Synchrotron Radiation Facility (SSRF) is the only third-generation accelerator light source in China, and its X-ray test beamline, which is a BM radiation source [32] with a broad X-ray spectrum, large experimental space, and high experimental flexibility, is a good choice for the first X-ray polarimeter research in China.

In this study, we designed and built a high-precision X-ray polarimeter consisting mainly of two channel-cut crystals used as a polarizer and analyzer, a high-precision motion-controlling mechanism, and a high-sensitivity detection system. With the help of precise electron orbit alignment and photon energy calibration technology, the polarization purity of 8.4×10^{-9} was achieved at an X-ray energy of 12.914 keV, which established the foundation for vacuum birefringence experiments in China based on a free-electron laser (FEL) [33] and 100 PW lasers [34].

2 Theory

The polarization direction can be defined for the electric radiation field. For a general BM source, the electric field is parallel to the plane of the electron orbit in the orbit plane, producing a horizontal polarization, or σ-mode. Above and below the plane, the electric field has a component perpendicular to the orbit plane, producing a vertical polarization, or π-mode. The angular distribution of the different polarized photon fluxes follows the modified Bessel functions $K_{1/3}$ and $K_{2/3}$, and the intrinsic polarization purity of the SR is defined as the ratio of the polarized components parallel and normal to the diffraction plane [35]:

$$N_{\sigma}(\psi) \propto K_{2/3}^{2}(\xi)$$

$$N_{\pi}(\psi) \propto \frac{\gamma^{2}\psi^{2}}{1+\gamma^{2}\psi^{2}} K_{1/3}^{2}(\xi)$$

$$\xi = \frac{1}{2}\frac{\omega}{\omega_{c}}(1+\gamma^{2}\psi^{2})^{3/2}$$

$$\delta_{\text{int}}(\psi) = \frac{N_{\pi}(\psi)}{N_{\sigma}(\psi)} \qquad (1)$$

where ω and ω_c are the photon frequency and critical photon frequency, respectively, γ is the relativistic Lorentz factor of the electrons, and ψ is the vertical angle of the photons departing from the orbit plane. Fig. 1(a) shows the angular distribution of photon flux percentage in different polarization states of the SR from the BM source, in which the horizontal axis is the vertical angle of the photons' departure from the electron orbit plane, the left vertical axis is the photon flux percentage of σ-mode and π-mode polarization, and the right vertical axis is the intrinsic polarization purity of the SR. Fig. 1(a) shows that the spatial distribution of the σ-polarized photons is directed mainly toward the orbital plane, and its flux drops rapidly off the plane. In Fig. 1(a), the flux percentage of the σ-polarized photons is over 99% within a 10 μrad departure from the orbital plane. Then, the photon flux drops rapidly from 99% to 1% within 10 to 200 μrad and even below 1% when the vertical angle exceeds this range. Therefore, it is important to precisely align the orbit plane for maximum σ-polarized photon flux and, consequently, for optimal linear polarization purity. In contrast, Fig. 1(a) shows that the intrinsic polarization purity of the SR decreases even more rapidly off the orbital plane. In Fig. 1(a), the vertical angle of the photons departing from the orbital plane must be restricted to the order of nanoradians to reach an intrinsic polarization purity of the 10^{-10} level, which is almost impossible for the BM source. Generally, the acceptance angle of the Si(111) monochromator is about 20 μrad (ψ = 10 μrad), and the corresponding polarization purity of the diffraction beam is only about 3‰. Therefore, it is impossible to obtain an SR with extremely high polarization purity using slits or ordinary monochromators.

The limit of polarization purity that can be reached based on crystal diffraction is determined by the dynamic theory of X-ray diffraction [36], which can be expressed as:

$$\delta_{\text{lim}} = \frac{\sqrt{|\gamma| |\chi_h|^2}}{|\tan 2\theta_{\text{B}}|} \qquad (2)$$

where γ is the asymmetry factor, χ_h is the dielectric susceptibility, and θ_B is the Bragg angle. At the Bragg angle of exactly 45°, the diffracted X-ray is totally σ-polarized, and the corresponding Bragg angle is called the polarization angle or Brewster angle. Fig. 1(b) shows the theoretical limit of the polarization purity based on crystal-Bragg diffraction for different angle deviations from the Brewster angle, in which the horizontal coordinate is the angle deviation from the Brewster angle, the vertical axis is the theoretical limit of the polarization purity for the Si(800) diffraction in the symmetric-Bragg configuration ($\gamma = -1$, $\chi_h = 1.8 \times 10^{-6}$), and both horizontal and vertical coordinates are logarithmic coordinates. Fig. 1(b) shows that the limit of the polarization purity achieved is quite sensitive to the angle/energy deviation from the Brewster angle/energy. For example, the angle deviation must not exceed 0.0016° to make sure the polarization purity is better than the 10^{-10} level, and the corresponding energy deviation should not exceed 360 meV according to the differential form of Bragg's equation, i.e., $\dfrac{\Delta\theta}{\tan\theta_B} = \dfrac{\Delta E}{E_B}$, in which $\Delta\theta = |\theta - \theta_B|$, $\Delta E = |E - E_B|$, θ_B / E_B is the Brewster angle/energy and $\Delta\theta \, / \, \Delta E$ is the angle/energy deviation from the Brewster angle/energy. Therefore, a high-precision angle/energy calibration is essential for improving the theoretic limit of polarization purity.
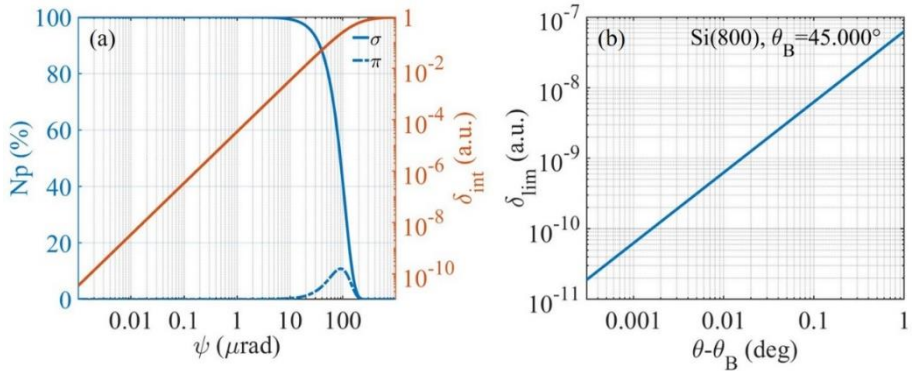

Fig. 1 (a) The angular distribution of photon flux percentage in different polarization states of the SR from the BM source, in which the horizontal coordinate is logarithmic and represents the vertical angle of the photon departure from the electron orbit plane, the left vertical axis represents the photon flux percentage of σ-mode and π-mode, and the right vertical axis represents the intrinsic polarization purity of the SR.

(b) The theoretical limit of the polarization purity based on crystal-Bragg diffraction for different angle deviations from the Brewster angle, in which both horizontal and vertical coordinates are logarithmic coordinates, the horizontal coordinate represents the angle deviation from the Brewster angle, and the vertical axis represents the theoretical limit of the polarization purity for the Si(800) diffraction.

3 Experiments and results

The experiments were conducted at the BL09B X-ray test beamline of the SSRF, which is a BM source with a critical energy of 10 keV [37]. The experiment was divided into four parts: crystal quality characterization, electron orbit alignment, photon energy calibration, and polarization purity measurement.

3.1 Crystal quality characterization

Perfect polarization requires perfect channel-cut crystals. On the one hand, channel-cut crystals can perform multiple reflections without changing the direction of the light, which reduces the number of crystals required and the difficulty of crystal adjustment. On the other hand, high reflectivity allows for a high transmission efficiency of the X-ray, even for multiple reflections. Therefore, it is necessary to characterize the quality of the channel-cut crystals used as polarizers and analyzers.

The optical layout of the crystal quality characterization is shown in Fig. 2(a). Two grooves with different widths were cut into a monolithic crystal to facilitate adjustment and measurement, allowing 4-reflections, 6-reflections, and 8-reflections, respectively. The channel-cut crystal was placed on a high-precision turntable (KOHZU, KTG-16W, 0.0025 arcsec/step) that was fixed in a high-load X-Z motorized stage (KOHZU, KHI-4SK, 1 μm resolution and 100 mm stroke). At the end of the light path, approximately 40 m from the light source, two different detectors were used to record the experimental data. A photodiode detector (PD, Hamamatsu, S3584-08) with a noise floor of ~ 0.1 pA was employed to measure the rocking curves (RCs) of the 6- and 8-reflection beam, and the reflectivity was calculated using the formula $R=\sqrt{I_8/I_6}$, where I_6 and I_8 are the peak intensities of the 6- and 8-reflection RC, respectively. In addition, a CCD camera (XIMEA, MH160XC-KK-FA) with a resolution of 7.4 μm/pixel was used to

record the position and shape of the diffraction spots. First, the photon energy of the X-rays was adjusted to 12.914 keV based on the Si(111) plane diffraction of a double-crystal monochromator (DCM). The size of the incident beam was adjusted to 5 mm × 1 mm through the slit upstream of the DCM to ensure that the areas of the inner surfaces of the groove were sufficiently large. Subsequently, the position of the channel-cut crystal along the Z-axis and the incident angle of the beam around the X-axis were adjusted to ensure that the incident X-rays could be fully diffracted by the channel-cut crystal. The 6- and 8-reflection RCs were recorded by the PD, as shown in Fig. 2(b). Finally, the channel-cut crystal was rotated to the Bragg angle, and the diffraction spots of 6- and 8-reflections were recorded using the CCD, as shown in Fig. 2(c).
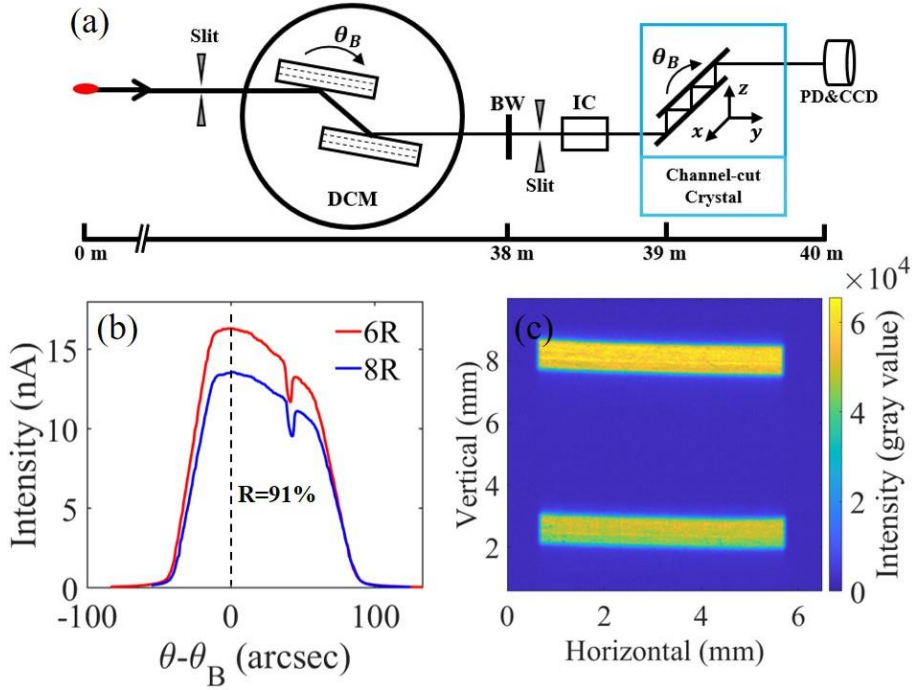

Fig. 2 (a) Optical layout of the crystal quality characterization of the polarimeter.

(b) RCs of the Si(800) diffraction of 6- and 8-reflections, in which the horizontal coordinate represents the angle deviation from the Bragg angle and the vertical axis represents the photocurrent intensity recorded by the PD.

(c) Spots of the Si(800) diffraction of 6- and 8-reflections, in which the horizontal and the vertical coordinates represent the horizontal and the vertical position in the CCD, respectively.

(DCM, double-crystal monochromator; BW, beryllium window; IC, ionization chamber; PD, photodiode detector).

Figs. 2(b) and 2(c) show the quality characterization results for the channel-cut crystal. Fig. 2(b) shows the RCs of the Si(800) crystal of 6- and 8-reflections, in which the horizontal coordinate is the deviation from the Bragg angle and the vertical axis is the photocurrent intensity recorded by the PD. Fig. 2(b) shows that the peak intensities of the 6- and 8-reflections RC are 16.3 nA and 13.6 nA, respectively; therefore, the reflectivity calculated is higher than 90%. Additionally, each RC includes a distinct glitch derived from multiple-beam diffraction, which can be eliminated by selecting an appropriate in-plane crystal angle. Fig. 2(c) shows the spots of the Si(800) diffraction of 6- and 8-reflections, where the horizontal and vertical coordinates are the horizontal and vertical positions in the CCD, respectively. The imaging results in Fig. 2(c) indicate that the sizes and shapes of the two diffraction beams were the same as those of the incident beam, demonstrating that the X-rays were successfully transmitted into the groove of the channel-cut crystal. Additionally, the beam position in Fig. 2(c) shows that the height of the 6-reflections beam is higher than that of the 8-reflections beam, due to the wider groove width of the 6-reflections.

3.2 Electron orbit alignment

Considering the polarization characteristics of the BM source, as discussed in section 2, and the narrow acceptance angle of the polarizer, it is essential to align the orbital plane precisely for optimal linear polarization purity.

The optical layout of the electron orbit alignment is shown in Fig. 3(a). The orbit analyzer was a flat Si(800) crystal that was placed on a turntable (KOHZU, RA10A-W01, 20-subdivision settings with 0.36" resolution) approximately 40 m downstream from the BM source. The diffraction plane of the orbit analyzer was perpendicular to that of the DCM. In this configuration, the π-polarized photons can be fully reflected, and the σ-polarized photons are greatly suppressed. As described in section 2, the photons are σ-polarized in the electron orbit plane, while the π-polarized photons are present above and below the orbital plane. Therefore, if the incident beam contains photons emitted from the electron orbit plane, there must be a dark area at the center of the diffraction spot. At the beginning of the experiment, two slits upstream and downstream of the DCM were fully opened to obtain the maximum photon flux at an

energy of 12.914 keV and to maximize the efficiency of alignment. Next, the orbit analyzer was rotated to the Bragg angle, and the CCD camera at the end of the optical path was used to record the diffraction spot of the orbit analyzer, as shown in Fig. 3(b). Finally, the vertical size of the slit downstream of the DCM was gradually narrowed to only about 0.5 mm around the orbital plane according to the intensity distribution of the diffraction spot in the vertical direction, and the CCD camera was used to record the diffraction spot of the orbit analyzer, as shown in Fig. 3(c).
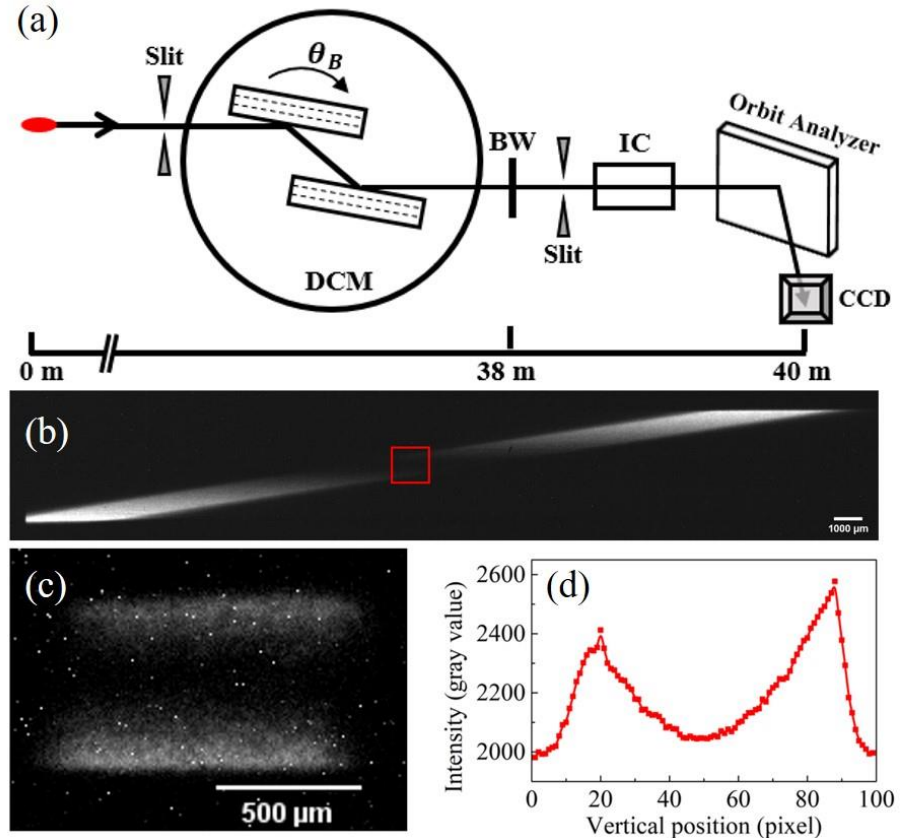
Fig. 3 (a) Optical layout of the electron orbit alignment.

Results for (b) diffracted spots and (c) central dark areas.

(d) Intensity distribution of the center dark area in the vertical direction, where the horizontal coordinate represents the vertical position of the spots in the CCD and the vertical axis represents the photocurrent intensity expressed by the gray value.

(DCM, double-crystal monochromator; BW, beryllium window; IC, ionization chamber).

The results of the electron orbit alignment are shown in Figs. 3(b) and 3(c). The results in Fig. 3(b) show that the size of the diffracted spots is approximately 30 mm × 4 mm, which is consistent with the size of the incident beam determined by the slit

upstream of the DCM. Fig. 3(c) shows the enlarged diffraction spots, including the dark center area, marked by the red rectangle in Fig. 3(a). Figure 3(d) shows the intensity distribution of the center dark area in the vertical direction, where the horizontal coordinate is the vertical position of the spots in the CCD and the vertical axis is the photocurrent intensity expressed by the gray value. Figure 3(d) shows that the vertical size of the dark area, i.e., the distance between the two peaks, was approximately 0.5 mm. Considering the incident beam flux, angular divergence, and crystal bandwidth, the final size of the incident beam is limited to approximately 1 mm × 0.5 mm centered on the orbit plane of the electrons, as shown in Fig. 3(c), and the corresponding angular divergence is 25 μrad × 12.5 μrad in the horizontal and vertical directions. The intrinsic linear polarization purity within the 0.5 mm range of the orbit plane is about 1‰ according to formula 1; however, the theoretical limit of the polarization purity restricted by angular divergence in this condition can reach 10^{-10} level, which can be demonstrated by $\delta \approx \sigma_H^2 + \sigma_V^2$ [38], where σ_H and σ_V are the horizontal and vertical divergence angles, respectively.

3.3 Photon energy calibration

Given the polarization characteristics of crystal diffraction, as discussed in section 2, the limit of the polarization purity achieved is sensitive to the angle/energy deviation from the Brewster angle/energy. Therefore, it is essential to calibrate the photon energy precisely for maximum polarization purity.

The optical layout of the photon-energy calibration is shown in Fig. 4(a). The white beam generated by the BM was monochromatized to approximately 12.914 keV based on the Si(111) plane diffraction in DCM. In order to achieve high-precision calibration, a V-shape crystal having two orthogonal Si(800) and Si(080) planes with an equal Darwin width of about 0.72″ was employed as the energy analyzer, providing an energy resolution of 45 meV to calibrate the X-ray energy passed through the polarizer. The polarizer and the energy analyzer were each placed on a high-precision turntable (KOHZU, KTG-16W, 0.0025 arcsec/step), fixed on a high-load X-Z motorized stage (KOHZU, KHI-4SK, 1 μm resolution, and 100 mm stroke). At first, the polarizer was

rotated around the 45° Brewster angle to obtain the RC recorded by the PD after the polarizer, as shown in Fig. 4(b). The Bragg angle of the polarizer was set at the center of the flat-top part of the RC. Subsequently, the polarizer and energy analyzer were configured in a dispersion (+--+) arrangement, and the Bragg angle of the energy analyzer was rotated to obtain the RC, as shown in Fig. 4(c). Next, the DCM was rotated in steps of 1″ (corresponding to an energy resolution of 63 MeV), and the energy analyzer was used to calibrate the photon energy passing through the polarizer accurately using the maximum RCs of the energy analyzer, as shown in Fig. 4(c).
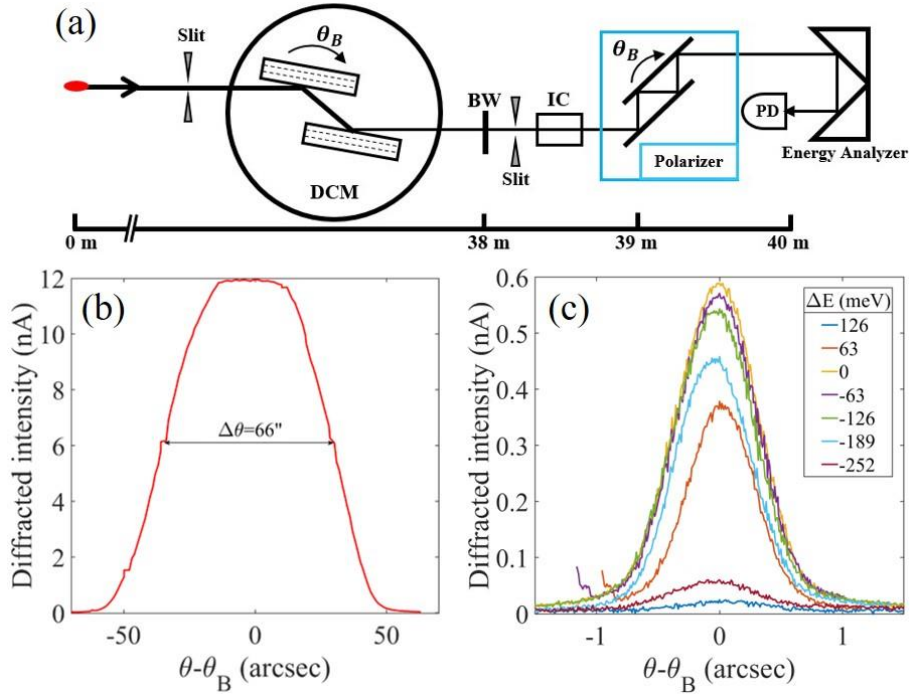
Fig. 4 (a) Optical layout of the photon energy calibration.

(b) RC of the polarizer at around 12.914 keV before energy calibration, in which the horizontal coordinate represents the angle deviation from the Bragg angle and the vertical axis represents the photocurrent intensity recorded by the PD.

(c) RCs of the analyzer at different photon energies around 12.914 keV after energy calibration, in which the horizontal coordinate represents the angle deviation from the Bragg angle and the vertical axis represents the photocurrent intensity recorded by the PD; RCs in different colors indicate different energy deviations.

(DCM, double-crystal monochromator; BW, beryllium window; IC, ionization chamber; PD, photodiode detector).

Fig. 4(b) shows the RC of the polarizer at approximately 12.914 keV before energy calibration, in which the horizontal coordinate is the angle deviation from the Bragg angle and the vertical axis is the photocurrent intensity recorded by the PD. Fig. 4(b) demonstrates that the angular width (FWHM) of the polarizer RC is about 66″, much larger than the 4.1″ Darwin width of the Si(111), and cannot meet the angle/energy accuracy requirement of the polarizer (no more than 0.002°/7.2″), as discussed in section 2. Fig. 4(c) shows the RCs of the analyzer at different photon energies of approximately 12.914 keV after energy calibration, in which the horizontal coordinate is the angle deviation from the Bragg angle, the vertical axis is the photocurrent intensity recorded by the PD, and RCs in different colors indicate different energy deviations. The angular width (FWHM) of each RC in Fig. 4(c) is about 0.72″, and the corresponding energy bandwidth is about 45 meV, which is consistent with the Darwin width of the Si(800) plane. The calibration accuracy of the energy analyzer is almost one order of magnitude more precise than that of the absorbing edge [39]. It can reach the level of the energy bandwidth of the Si(800) plane, which is sufficient to obtain a linearly polarized beam with a polarization purity better than that of 10^{-10}, according to Fig. 1(b).

3.4 Polarization purity measurement

The position and size of the SR beam were limited to approximately 1 mm × 0.5 mm centered on the electron orbit plane after orbital alignment, and the photon energy was calibrated to 12.914 keV with an energy bandwidth better than 50 meV. Therefore, the theoretical limit of the polarization purity in such a situation can reach the 10^{-10} level, as previously discussed.

The optical layout of the polarization purity measurement setup is shown in Fig. 5(a). An ionization chamber (IC) was installed before the polarizer to monitor the beam intensity during the experiments. The polarizer was positioned close to the beryllium window (BW) of the beamline, whereas the analyzer was positioned approximately 5 m downstream of the polarizer to suppress background radiation efficiently. Moreover, the position and angle of the polarizer crystal were adjustable in seven dimensions,

including crystal translation along the X-, Y-, and Z-axes related to the crystal turntable, crystal rotation of the pitch angle (Bragg angle), yaw angle (in-plane angle), and translation of the crystal turntable along the X- and Z-axes. In contrast, the adjustment mechanism of the analyzer crystal was more complicated and included three additional rotations of the crystal turntable, including the pitch angle (around the X-axis), yaw angle (around the Z-axis), and roll angle (around the Y-axis, defined as the analyzer angle which is the angle between the two diffraction planes of the analyzer and polarizer crystals). The adjustment accuracy and range of the pitch-, yaw-, and roll-angles were 0.004″ in $\pm 5°$, 072″ in $\pm 2°$, and 072″ in $\pm 175°$, respectively. The polarimeter system comprised 12 reflections: four in the polarizer crystal to adequately suppress π-mode photons while ensuring reasonable transmission of σ-mode photons, and eight in the analyzer crystal to minimize scattering photons as much as possible. The scanning range of the analyzer angle was $0° \sim 95°$; the $0°$ and $90°$ positions denoted the parallel and perpendicular positions of the two diffraction planes of the polarizer and analyzer crystals, respectively. First, the polarizer and analyzer were preliminarily aligned using a laser to ensure that the bases of the two channel-cut crystals were at the same height as the incident beam. Subsequently, the SR beam was limited to approximately 1 mm × 0.5 mm, centered on the electron orbit plane, and the photon energy was calibrated to 12.914 keV, as discussed previously. Meanwhile, the Bragg angle of the polarizer was maintained at $45.002°$ with an appropriate in-plane angle to avoid the effect of multiple-beam diffraction. Subsequently, the position and altitude of the analyzer were adjusted to ensure that the SR beam was perpendicular to the turntable plane of the roll angle and through its rotation center, which was indispensable for guaranteeing the same Bragg angle of the analyzer crystal over the scanning range of the analyzer angle. Finally, the analyzer angle was rotated from $0°$ to $95°$, and three different detectors were used to record the signals: a PD was used to measure the RCs of the analyzer at different analyzer angles from $0°$ to $85°$, a homemade avalanche photodiode detector (APD) was used to measure the RCs from $85°$ to $89.97°$, and a two-dimensional single photon detector (2D-SPD, SPECTRUM, Lambda 250K) was placed behind the analyzer to record the intensity, shape, and position of the exit beam at each analyzer angle. The

integration time of the 2D-SPD was varied from 1 s to 10000 s to avoid signal saturation of the detector and obtain sufficient photons, depending on the analyzer angles.
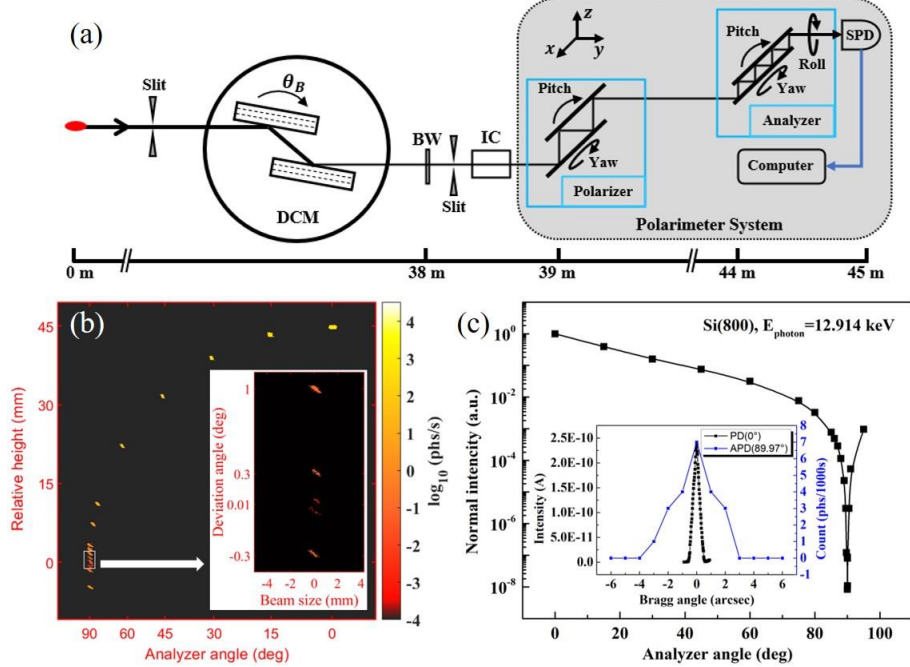

Fig. 5 (a) Optical layout of the polarization purity measurement.

(b) The spots of the diffracted beam from the polarimeter system, in which the horizontal coordinate represents the analyzer angle of the analyzer crystal and the vertical axis represents the relative height of the diffracted beam imaged by the 2D-SPD. The color bar represents the photon counts of the spots, and logarithmic coordinates are taken because of the large range. The inner figure shows the partially enlarged drawing around the perpendicular position, in which the horizontal coordinate represents the beam size of the diffracted beam and the vertical axis represents the deviation angle from the 90° analyzer angle, i.e., the perpendicular position.

(c) The polarization purity measurement results of the polarimeter system, in which the horizontal coordinate represents the analyzer angle of the analyzer crystal and the vertical axis represents the normal intensity of the diffracted beam, i.e., the polarization purity of the exit beam. The inner graph is the Bragg angle peaks of the RCs at the parallel position and the perpendicular position, in which the horizontal coordinate represents the angle deviation from the Bragg angle and the vertical axis represents the photocurrent intensity of the diffracted beam recorded by the PD and APD.

(DCM, double-crystal monochromator; BW, beryllium window; IC, ionization chamber;

Fig. 5(b) shows the spot distribution of the diffracted beam from the polarimeter system, in which the horizontal coordinate is the analyzer angle of the analyzer crystal and the vertical axis is the relative height of the diffracted beam imaged by the 2D-SPD. Each spot was imaged at the Brewster angle of the analyzer, corresponding to the maximum RC at each roll angle position, and the final results were normalized to the integration time. The analyzer rotation radius of the roll angle was 45 mm, creating a 45 mm relative height between the parallel and perpendicular positions. The maximum photon flux (0° roll angle) entering the 2D-SPD was approximately 3 million photons/s in the parallel position. The exposure time was set to the maximum achievable limit of 10000 s at the current noise floor of the 2D-SPD to collect a credible number of photons near the perpendicular position. A photon flux of 25 photons/10000 s was recorded at the perpendicular position, and the uncertainty caused by background noise was approximately 1 photons/10000 s. As shown in Fig. 5(b), the measurement results indicate that the intensity range of the 21 spots spans more than eight orders of magnitude as the analyzer moves from 0° to 95°, and each spot is a Dumond diagram of the diffraction beam. Meanwhile, the inclined angles between the DuMond diagrams and the horizontal direction gradually approached 35°, as demonstrated more clearly in the inner figure, which is a partially enlarged drawing near the perpendicular position, in which the horizontal coordinate is the beam size of the diffracted beam and the vertical axis is the deviation angle from the 90° analyzer angle, i.e., the perpendicular position. This follows the dynamic theory of X-ray diffraction based on orthogonal crystals [40], where the inclined angle of the Dumond diagram for the horizontal direction can be expressed as $\alpha = \tan^{-1} \dfrac{\sin \theta_{B,p} \tan \theta_{B,p}}{\tan \theta_{B,a}}$. $\theta_{B,\mathrm{p}}$ and $\theta_{B,a}$ are the Bragg angles of the polarizer and analyzer, respectively, at a given X-ray energy. Therefore, we can obtain $\alpha = 35^{\circ}$ when the X-ray arrives at the Brewster angles for polarizer and analyzer crystals ($\theta_{B,p} = \theta_{B,a} = 45^{\circ}$).

Fig. 5(c) shows the result of the polarization purity measurement, i.e., a quantitative

analysis of the spot integral intensities in Fig. 5(b), in which the horizontal coordinate is the analyzer angle of the analyzer crystal and the vertical axis is the spot distribution of the diffracted beam imaged by the 2D-SPD. The inner graph in Fig. 5(c) depicts the Bragg angle peaks of the RCs in the parallel position and near the perpendicular position, where the horizontal coordinate represents the angle deviation from the Bragg angle and the vertical axis represents the photocurrent intensity of the diffracted beam recorded by the PD and APD. The inner graph reveals that the Bragg angle of the RC peak at the parallel position is shifted by less than 1°, indicating that we achieved satisfactory parallelism between the X-ray beam and the axis of the roll angle (analyzer angle). Furthermore, the width (FWHM) of the RC is quite close to the theoretical limit of the Darwin width of the Si(800) plane at the parallel position, increasing to about 3.5″ while moving to the perpendicular position. This is partly due to the perfect crystal quality of the excellent processing technology, which minimized the bandwidth expansion caused by lattice deformation during the diffraction process. Also, high-precision electron orbit alignment and photon energy calibration technologies make it possible to achieve a small angle divergence of less than 25 μrad and a small energy deviation of less than 50 meV. Notably, the transmission efficiency of the system can exceed 20% within the bandwidth of the polarizer and analyzer due to high-quality crystals with a reflectivity of more than 90%. Finally, the intensity was normalized for the incident photon flux, and the result indicates that the flux of the π-mode photons can be suppressed by a factor of 8.4×10^{-9}.

4 Conclusion

We designed and built a high-precision X-ray polarimeter based on multiple Brewster reflections of channel-cut crystals at an energy of 12.914 keV. A 2D-SPD was employed to record the shape and intensity of the diffracted beam. The measured polarization purity was 8.4×10^{-9} using precise electron orbit alignment and photon energy calibration technology, a significant step in exploring vacuum birefringence in China. Polarization purity is mainly limited by the brightness of the BM source, which is several orders of magnitude less than that of the undulator source. In time, a polarization purity better than $\sim 10^{-10}$ can be expected based on X-ray sources with

higher brightness and lower divergence angle, such as DLSRs and FELs, and further improvements to X-ray polarimeters, such as using different crystals with lower atomic numbers.

References

1. C.G. Barkla, Polarisation in Röntgen Rays. Nature **69**, 463 (1904). https://doi.org/10.1038/069463a0

2. K.S. Schulze, R. Loetzsch, R. Rüffer et al., X-ray dichroism in polyimide caused by non-resonant scattering. J. Synchrotron Radiat. **28**, 176-180(2021). https://doi.org/10.1107/S1600577520015568

3. M. Hart, X-ray polarization phenomena. Philos. Mag. B **38**, 41-56 (1978). https://doi.org/10.1080/13642817808245319

4. S. Mukherjee, J.K. Streit, E. Gann et al., Polarized X-ray scattering measures molecular orientation in polymer-grafted nanoparticles. Nat. Commun. **12**, 4896 (2021). https://doi.org/10.1038/s41467-021-25176-4

5. L. Paolasini, C. Detlefs, C. Mazzoli et al., ID20: a beamline for magnetic and resonant X-ray scattering investigations under extreme conditions. J. Synchrotron Radiat. **14**, 301–312 (2007). https://doi.org/10.1107/S0909049507024879

6. E.E. Alp, W. Sturhahn, T.S. Toellner et al., Vibrational Dynamics Studies by Nuclear Resonant Inelastic X-Ray Scattering. Hyperfine Interact. **144**, 3-20 (2002). https://doi.org/10.1023/A:1025452401501

7. E.E. Alp, W. Sturhahn and T.S. Toellner, Polarizer–analyzer optics. Hyperfine Interact. **125**, 45-68 (2000). https://doi.org/10.1023/A:1012673301869

8. G. van der Laan and A. I. Figueroa, X-ray magnetic circular dichroism-A versatile tool to study magnetism. Coord. Chem. Rev. **277-278**, 95-129 (2014). https://doi.org/10.1016/j.ccr.2014.03.018

9. A. Ney, V. Ney, K. Ollefs et al., X-Ray Linear Dichroism: An Element-Selective Spectroscopic Probe for Local Structural Properties and Valence. J. Surf. Interfaces Mater. **2**, 14-23 (2014). https://doi.org/10.1166/jsim.2014.1031

10. T. Heinzl, B. Liesfeld, K. U. Amthor et al., On the observation of vacuum birefringence. Opt. Commun. **267**, 318-321 (2006). https://doi.org/10.1016/j.optcom.2006.06.053

11. F. Karbstein, H. Gies, M. Reuter et al., Vacuum birefringence in strong inhomogeneous electromagnetic fields. Phys. Rev. D **92**, 071301 (2015). https://doi.org/10.1103/PhysRevD.92.071301

12. H.P. Schlenvoigt, T. Heinzl, U. Schramm et al., Detecting vacuum birefringence with x-ray free electron lasers and high-power optical lasers: a feasibility study. Phys. Scr. **91**, 023010 (2016). https://doi.org/10.1088/0031-8949/91/2/023010

13. F. Karbstein, Vacuum birefringence in the head-on collision of X-ray free-electron laser and optical high-intensity laser pulses. Phys. Rev. D **98**, 056010 (2018). https://doi.org/10.1103/PhysRevD.98.056010

14. J. J. Klein and B. P. Nigam, Birefringence of the Vacuum. Phys. Rev. **135**, B1279 (1964). https://doi.org/10.1103/PhysRev.135.B1279

15. C.G. Barkla, Polarisation in Rontgen Rays. Nature **69**, 1904 (1794). https://doi.org/10.1038/069463a0

16. W. Friedrich, P. Knipping, M. von Laue, Interferenzerscheinungen bei Rontgenstrahlen. Ann. Der Phys. **346**, 971-988 (1913). https://doi.org/10.1002/andp.19133461004

17. C.G. Darwin, The Theory of X-Rag Reflexion. Philos. Mag. **27**, 315-333 (1914). https://doi.org/10.1080/14786440208635093

18. H. Cole, F. W. Chambers and C. G. Wood, X-Ray Polarizer. J. Appl. Phys. **32**, 1942-1945 (1961). https://doi.org/10.1063/1.1728267

19. A. Authier, S. Lagomarsino and B. K. Tanner. X-Ray and Neutron Dynamical Diffraction. 1st edn. (Springer, New York, 1996), pp. 91-109. https://doi.org/10.1007/978-1-4615-5879-8

20. D.P. Siddons, I.M. Hart, Y. Amemiya et al., X-Ray Optical Activity and the Faraday Effect in Cobalt and Its Compounds. Phys. Rev. Lett. **64**, 1967-1970 (1990). https://doi.org/10.1103/PhysRevLett.64.1967

21. R. Röhlsberger, E. Gerdau, R. Rüffer et al., X-ray optics for mu eV-resolved spectroscopy. Nucl. Instrum. Meth. A **394,** 251-255 (1997). https://doi.org/10.1016/S0168-9002(97)00710-9

22. B. Marx, I. Uschmann, S. Höfer et al., Determination of high-purity polarization state of X-rays. Opt. Commun. **284**, 915-918 (2011). https://doi.org/10.1016/j.optcom.2010.10.054

23. B. Marx, K.S. Schulze, I. Uschmann et al., High-Precision X-Ray Polarimetry. Phys. Rev. Lett. **110**, 254801 (2013). https://doi.org/10.1103/PhysRevLett.110.254801

24. K.S. Schulze, B. Grabiger, R. Loetzsch et al., Towards perfectly linearly polarized X-rays. Phys. Rev. Res. **4**, 013220 (2022). https://doi.org/10.1103/PhysRevResearch.4.013220

25. H.X. Yin, J.B. Guan, S.Q. Tian et al., Design and optimization of diffraction-limited storage ring lattices based on many-objective evolutionary algorithms. Nucl. Sci. Tech. **34**, 147 (2023). https://doi.org/10.1007/s41365-023-01284-2

26. J. Chen, Y.B. Leng, L.Y. Yu et al., Optimization of the cavity beam-position monitor system for the Shanghai soft X-ray free-electron laser user facility. Nucl. Sci. Tech. **33**, 124 (2022). https://doi.org/10.1007/s41365-022-01117-8

27. Z.Y. Ma, S.J. Zhao, X.M. Liu et al., High RF power tests of the first 1.3 GHz fundamental power coupler prototypes for the SHINE project. Nucl. Sci. Tech. **33**, 10 (2022). https://doi.org/10.1007/s41365-022-00984-5

28. J. Yang, Y.C. Du, L.X. Yan et al., Laser–RF synchronization based on digital phase detector. Nucl. Sci. Tech. **28**, 57 (2017). https://doi.org/10.1007/s41365-017-0205-z

29. C. Jiang, Z.X. Zhang, H. Dong et al., Generation and application of high-contrast laser pulses using plasma mirror in the SULF-1PW beamline. Chin. Opt. Lett. **21**, 043802 (2023). https://doi.org/10.3788/COL202321.043802

30. X.M. Lu, X.Y. Liang, Y.X. Leng et al., Improvement of the large aperture Ti:sapphire amplifiers in the petawatt femtosecond laser system at SIOM. Chin. Opt. Lett. **8**, 1008 (2010). https://doi.org/10.3788/COL20100810.1008

31. H.T. Li, B. Zhao, X.Z. Zhang et al., Development of a portable laser heating device for synchrotron radiation in situ experiment. Nucl. Tech. **46**, 020101 (2023). http://doi.org/10.11889/j.0253-3219.2023.hjs.46.020101

32. J. Eberhard, Jaeschke, K. Shaukat, Jochen R. et al., Synchrotron Light Sources and Free-Electron Lasers. 2nd edn. (Springer, Switzerland, 2020), pp. 20-21. https://doi.org/10.1007/978-3-030-23201-6

33. N.S. Huang, Z.P. Liu, B.J. Deng et al., The MING proposal at SHINE: megahertz cavity enhanced X-ray generation. Nucl. Sci. Tech. **34**, 6 (2023). https://doi.org/10.1007/s41365-022-01151-6

34. B.F. Shen, Z.G. Bu, J.C. Xu et al., Exploring vacuum birefringence based on a 100 PW laser and an x-ray free electron laser beam. Plasma Phys. Control. Fusion. **60**, 044002 (2018). https://doi.org/10.1088/1361-6587/aaa7fb

35. J. Eberhard, Jaeschke, K. Shaukat, Jochen R. et al., Synchrotron Light Sources and Free-Electron Lasers. 2nd edn. (Springer, Nature Switzerland, 2020), pp. 57-58. https://doi.org/10.1007/978-3-030-23201-6

36. A. Authier. International Tables for Crystallography. (Springer, Dordrecht, 2010). Vol. B, Chapter 5.1, pp. 626–646. https://doi.org/10.1107/97809553602060000108

37. Z.L. Li, Y.C. Fan, L. Xue et al., The design of the Test Beamline at SSRF. In 13th International Conference on Synchrotron Radiation Instrumentation (SRI2018), 2054,

(2019). https://doi.org/10.1063/1.5084671

38. K.S. Schulze, Fundamental limitations of the polarization purity of X rays. APL Photonics. **3**, 126106 (2018). https://doi.org/10.1063/1.5061807

39. Z.L. Li, J.L. Yang, S.Y. Si et al., Simple, high-resolution method for measurement of the natural relative energy bandwidth of Si(111) double crystal monochromators. Nucl. Instrum. Meth. A **983**, 164526 (2020). https://doi.org/10.1016/j.nima.2020.164526

40. M. Servidori, F. Cembali and S. Milita, 3D DuMond diagrams of multi-crystal Bragg-case synchrotron topography. I. Flat sample. Appl. Phys. A **73**, 75-82 (2001). https://doi.org 10.1007/s003390100843